Check for updates

JGR Oceans

RESEARCH ARTICLE

10.1029/2025JC023272

# Distribution of Plastics of Various Sizes and Densities in the Global Ocean From a 3D Eulerian Model

**Zih-En Tseng[1], Yue Wu[1], Dimitris Menemenlis[2], Guangyao Wang[1], Chris Ruf[3], and Yulin Pan[1]**

[1]Naval Architecture and Marine Engineering, the University of Michigan, Ann Arbor, MI, USA, [2]Jet Propulsion Laboratory, California Institute of Technology, Pasadena, CA, USA, [3]Climate and Space Sciences and Engineering, the University of Michigan, Ann Arbor, MI, USA

**Key Points:**

- We develop a global 3D Eulerian model for oceanic microplastics transport, with particle size and density affecting the vertical transport
- For each choice of material density, the distribution depends on the size of particles, which is illustrated by the model
- Seasonal sea surface concentration variability is consistent with Cyclone Global Navigation Satellite System satellite observations and explained by ocean mixed layer depth

**Supporting Information:**

Supporting Information may be found in the online version of this article.

**Correspondence to:**

Y. Pan,
yulinpan@umich.edu

**Citation:**

Tseng, Z.-E., Wu, Y., Menemenlis, D., Wang, G., Ruf, C., & Pan, Y. (2025). Distribution of plastics of various sizes and densities in the global ocean from a 3D Eulerian model. *Journal of Geophysical Research: Oceans*, *130*, e2025JC023272. https://doi.org/10.1029/2025JC023272

Received 7 AUG 2025
Accepted 13 AUG 2025

**Author Contributions:**

**Conceptualization:** Chris Ruf, Yulin Pan
**Data curation:** Zih-En Tseng, Guangyao Wang, Chris Ruf
**Formal analysis:** Zih-En Tseng, Yue Wu, Chris Ruf, Yulin Pan
**Funding acquisition:** Chris Ruf, Yulin Pan
**Investigation:** Zih-En Tseng, Chris Ruf
**Methodology:** Zih-En Tseng, Yue Wu, Dimitris Menemenlis, Chris Ruf, Yulin Pan
**Project administration:** Chris Ruf, Yulin Pan
**Resources:** Dimitris Menemenlis, Chris Ruf, Yulin Pan

© 2025. The Author(s).
This is an open access article under the terms of the Creative Commons Attribution License, which permits use, distribution and reproduction in any medium, provided the original work is properly cited.

**Abstract** We study the global transport and distribution of microplastics (MPs) using a three-dimensional Eulerian model. For the first time, the effects of both particle size and density are accounted for, influencing the vertical transport of MPs, and leading to an advanced understanding of their global distribution. Our simulations reveal two key findings: Only particles with low density and sufficiently large size (e.g., density 900 kg $m^{-3}$ and size $\gtrsim$10 μm) aggregate in the five subtropical gyres that were identified in previous studies. In contrast, sufficiently small particles ($\lesssim$1 μm), regardless of their density, behave like neutrally buoyant particles and can penetrate down to 1 km deep into the ocean. In addition, we observe a seasonal variation in the surface concentration of positively buoyant MPs—higher in summer and lower in winter—which reasonably agrees with the satellite observations made by the Cyclone Global Navigation Satellite System (CYGNSS) in terms of the phase of the variation. A quantitative analysis shows that the seasonal variation in the surface particle concentration correlates well globally with the variation in mixed layer depth. We attribute this correlation to the vertical stretching/squeezing effect of the seasonally varying mixed layer, where the total amount of positively buoyant particles is conserved.

**Plain Language Summary** The oceanic plastic pollution is an urgent global problem. We study the transport and distribution of microplastics (plastic pieces with sizes smaller than 5 mm) using a newly developed computer simulation. The effect of plastic particle size is considered for the first time and found to affect the vertical motion of the particles. This consideration leads to new understanding of the microplastic distribution compared to previous studies. On one hand, only plastic particles made from low-density material with sufficient size ($\gtrsim$10 μm) accumulate in the five subtropical gyres, forming the garbage patches identified in previous studies. On the other hand, sufficiently small ($\lesssim$1 μm) plastic particles exhibit weaker surface patterns and can be found in the deeper oceans (up to about 1 km deep). Additionally, we find that the amount of floating plastics on the sea surface changes seasonally, generally with more in summer and less in winter. This seasonal pattern agrees with satellite observations made by the NASA Cyclone Global Navigation Satellite System (CYGNSS), which consists of eight microsatellites measuring ocean surface roughness. We explain the seasonal variation by physically connecting it to the seasonal variation in the mixed layer depth of the ocean.

## 1. Introduction

Plastic pollution in the ocean is a fundamental environmental problem we face now and will continue to face for the foreseeable future. An estimated 19–23 million tons of plastic trash enters the ocean each year (Borrelle et al., 2020; Lau et al., 2020), and many of it is battered by sun and ocean waves into microplastics (MPs), that is, plastic particles less than 5 mm long (Hartmann et al., 2019; the NOAA Marine Debris Program, 2024). These small pieces of plastics can easily enter the food chain and pollute the food we humans consume. MPs are also shown to play a role in climate change through their interaction with sea ice (Mountford & Morales Maqueda, 2021) and their release of greenhouse gases via microbial activities (Sunil et al., 2024). Therefore, it is crucial to understand the distribution of MPs in the global ocean for the strategic removal of their pollution.

A major method for field measurements of oceanic plastic concentration is by trawler nets, which capture particles of size greater than 0.2 mm floating near the ocean surface. Several studies (Cózar et al., 2014; Eriksen et al., 2014) have been done using this technique. However, the information gained is sparse in both space and time. Moreover, due to the limited measurement duration and spatial coverage, the results are sensitive to inhomogeneous disturbances such as eddies and surface wind (Lebreton et al., 2012). In contrast, remote sensing

**Software:** Zih-En Tseng, Dimitris Menemenlis, Guangyao Wang, Chris Ruf
**Supervision:** Yue Wu, Dimitris Menemenlis, Chris Ruf, Yulin Pan
**Validation:** Zih-En Tseng, Yue Wu, Guangyao Wang, Chris Ruf, Yulin Pan
**Visualization:** Zih-En Tseng, Chris Ruf
**Writing – original draft:** Zih-En Tseng, Chris Ruf
**Writing – review & editing:** Zih-En Tseng, Yue Wu, Dimitris Menemenlis, Guangyao Wang, Chris Ruf, Yulin Pan

**Table 1**
*Summary of Features of Our Model and Previous Ones*

| Models | Velocity data source | Grid spacing | Model type |
|---|---|---|---|
| Our model | ECCOv4r4[a] | 37–110 km | 3D Eulerian |
| Richon et al. (2022) | NEMO[b] | 2° | 3D Eulerian |
| Chenillat et al. (2021) | GLORYS[c] | 1/12° | 2D Lagrangian |
| Mountford and Morales Maqueda (2019) | NEMO[d] | 1°−2° | 3D Eulerian |
| Lebreton et al. (2012) | HYCOM[e] | 1/12° | 2D Lagrangian |
| van Sebille et al. (2012) | GDP[f] | 1° | 2D statistical |
| Maximenko et al. (2012) | GDP | 1° | 2D statistical |

[a]Estimating the Circulation and Climate of the Ocean Version 4 Release 4. [b]Nucleus for European Modeling of the Ocean. [c]Global Ocean Physics Reanalysis. [d]Nucleus for European Modeling of the Ocean. [e]HYbrid Coordinate Ocean Model. [f]Global Drifter Program.

methods provide a much greater spatial coverage. Among several proposed techniques, Evans and Ruf (2022) retrieve the concentration of positively buoyant MPs from the ocean surface roughness anomaly (i.e., surface roughness lower than expected at a given wind speed), establishing the first database of MPs for the region covering 38°S to 38°N. While favorable agreement with other approaches has been reported, it should be noted that the retrieval algorithm relies on the presence of surfactants, which act as tracers to damp the surface roughness (Sun et al., 2023). Therefore, the results obtained need to be interpreted with caution due to the differences in transport mechanisms between MPs and surfactants.

Transport models for MPs offer another way to understand their global distribution. Existing global transport models are summarized and classified as two-dimensional (2D) Lagrangian, 2D statistical, and three-dimensional (3D) Eulerian models (Table 1). In 2D Lagrangian models, each particle released into the ocean is tracked as a passive scalar following the ocean surface current velocity, with the velocity obtained from global reanalysis data sets (Chenillat et al., 2021; Lebreton et al., 2012). In 2D statistical models, the surface concentration of MPs evolves by advection in a probabilistic way, with the probability calculated from the Global Drifter Program (GDP) (Maximenko et al., 2012; Niiler, 2001; van Sebille et al., 2012). Mountford and Morales Maqueda (2019) and Richon et al. (2022) present results from 3D Eulerian models of plastic particle concentrations by solving the advection-diffusion tracer equations in the global ocean. The two models differ regarding the calculation of the vertical terminal velocity: The former considers it to result from the density difference between particles and seawater, while the latter treats it as a preset constant. When the above 2D and 3D models are integrated for a sufficient time, it is usually found that the accumulation of particles, or of positively buoyant particles in the case of Mountford and Morales Maqueda (2019) and Richon et al. (2022), appear in five subtropical gyres as stationary patterns in the global ocean. However, none of the previous models consider the impact of particle size, which can affect the vertical motion of the particles. Furthermore, there is little study to explain the seasonal variability of surface concentration [except Richon et al. (2022) which will be discussed in §3.3], as predicted in van Sebille et al. (2012) and as observed in remote sensing data (Evans & Ruf, 2022).

In this paper, we continue the investigation of concentration of MPs in the global ocean using a 3D Eulerian model. Compared to 2D Lagrangian and statistical models, Eulerian models have the advantage that the computational cost does not increase with number of particles, since the particles are modeled as concentrations. Additionally, Eulerian models allow the parameterization of subgrid-scale processes, for example, mesoscale and submesoscale variability and vertical mixing. Compared to Mountford and Morales Maqueda (2019), the Eulerian model developed in this paper is associated with the advancements in both the ocean circulation data set and the formulation of the advection-diffusion equation. For the circulation data set, we use the Estimating the Circulation and Climate of the Ocean Version 4, Release 4 (ECCOv4r4) 1992–2017 state estimate, which is data-assimilated with most available global-ocean observations, instead of a free-running reanalysis, such as NEMO used in Mountford and Morales Maqueda (2019). In addition, unlike in NEMO where the "normal-year" atmospheric forcings are repeated over 50 years, the ECCOv4r4 data set fully preserves 26 years of interannual variability. These characteristics make the ECCOv4r4 solution uniquely well suited for ocean tracer studies. More importantly, for the formulation of the advection-diffusion equation, we use not only a mass-conserving form of the



21699291, 2025, 9, Downloaded from https://agupubs.onlinelibrary.wiley.com/doi/10.1029/2025JC023272 by University Of Michigan Library, Wiley Online Library on [30/08/2025]. See the Terms and Conditions (https://onlinelibrary.wiley.com/terms-and-conditions) on Wiley Online Library for rules of use; OA articles are governed by the applicable Creative Commons License

21699291, 2025, 9, Downloaded from https://agupubs.onlinelibrary.wiley.com/doi/10.1029/2025JC023272 by University Of Michigan Library, Wiley Online Library on [30/08/2025]. See the Terms and Conditions (https://onlinelibrary.wiley.com/terms-and-conditions) on Wiley Online Library for rules of use; OA articles are governed by the applicable Creative Commons License

buoyancy advection term in the model equation but also a robust formula to incorporate the effect of the particle size on the vertical terminal velocity. Both features are desirable advancements compared to Mountford and Morales Maqueda (2019).

Equipped with our new Eulerian model, we study the stationary distribution pattern of MPs with different properties (i.e., density and size) after integrating the model from 1992 to 2017. We find that only low-density particles (e.g., density $\rho_p = 900$ kg m$^{-3}$) with sufficiently large size (diameter $d \gtrsim 10$ μm) form the previously identified concentrations (a.k.a. "patches") in the five subtropical gyres. For particles smaller than some "critical size," which depends on their density, the distributions converge to that of neutrally buoyant particles with a much weaker surface accumulation pattern and a penetration into a greater depth of about 1 km. Here, the "critical size" is identified explicitly for each choice of particle density only because we incorporate the size effect into the terminal velocity. Additionally, for positively buoyant particles, we observe a seasonal variation of the surface concentration that agrees reasonably well with remote sensing data from the Cyclone Global Navigation Satellite System (CYGNSS) in terms of the phase of the cycle. The seasonal variability of surface concentration is found to be well correlated with that of the mixed layer depth (MLD) globally, based on which a physical explanation is developed. Specifically, as demonstrated in our model results, the positively buoyant particles have a nearly uniform distribution in the mixed layer (ML). Because of the mass conservation of particles in the ML, their surface concentration varies inversely proportional to the MLD.

This paper is organized as follows: In §2, we provide details of our MP transport model, including the model equation and formulation to incorporate the vertical motion and the terminal velocity, as well as details of the ECCOv4r4 state estimate. In §3, we show results of stationary patterns of the surface concentration of MP particles with different densities and sizes, with a focus on the effect of size on the distribution. The seasonal variation of the surface particles, their correlation with CYNGSS observations, and the underlying physical mechanism are discussed. Section §4 concludes the work and discusses possible directions for further improvements.

## 2. Methodology

We model the MP particles as passive tracers advected by ocean currents using the Massachusetts Institute of Technology general circulation model (MITgcm; Marshall, Adcroft, et al., 1997; Marshall, Hill, et al., 1997). The concentration of particles is described by the advection-diffusion equation with an additional term to represent the buoyancy effect,

$$\frac{\partial \tau}{\partial t} + \nabla \cdot (\tau \mathbf{u}) + \partial_z (\tau w_r) = \nabla \cdot (K \nabla \tau) + Q, \tag{1}$$

where $\tau$ is the particle concentration in g m$^{-3}$, $\nabla \equiv \frac{\partial}{\partial x}\hat{i} + \frac{\partial}{\partial y}\hat{j} + \frac{\partial}{\partial z}\hat{k}$ is the 3D gradient operator, with $x$, $y$ and $z$ being the three spatial dimensions and $\hat{i}$, $\hat{j}$, and $\hat{k}$ the unit vectors in each dimension, respectively. Vector $\mathbf{u}$ is the ocean current velocity taken from the ECCOv4r4 state estimate (described in §2.1). The term $\partial_z(\tau w_r)$ represents the buoyancy effect with $w_r$ being the vertical terminal velocity (described in §2.2). The diffusivity tensor $K$ is used to model unresolved processes (also described in §2.1). Finally, $Q$ is the source term distributed along coastlines based on Jambeck's global mismanaged waste survey (Figure 1; Jambeck et al., 2015), consistent with the coastal input used in van Sebille et al. (2012) and Mountford and Morales Maqueda (2019). The release totals up to 12.7 million tons of plastic debris entering the ocean each year, based on the estimation made by Jambeck et al. (2015).

In this work, Equation 1 is solved using the "ptracers" package in MITgcm, with necessary modifications to include the additional terms. Numerical setups for the simulation are summarized in §2.3, with key simulation files, result animations, and procedures made available and summarized in the section "Data Availability Statement." Animations of some simulation results are also uploaded as Supporting Information S1.

### 2.1. ECCOv4r4 Data Set

One of the important advancements of the current study relative to Mountford and Morales Maqueda (2019) is that we use the ECCOv4r4 solution, a data-assimilated ocean state estimate from 1992 to 2017 (ECCO

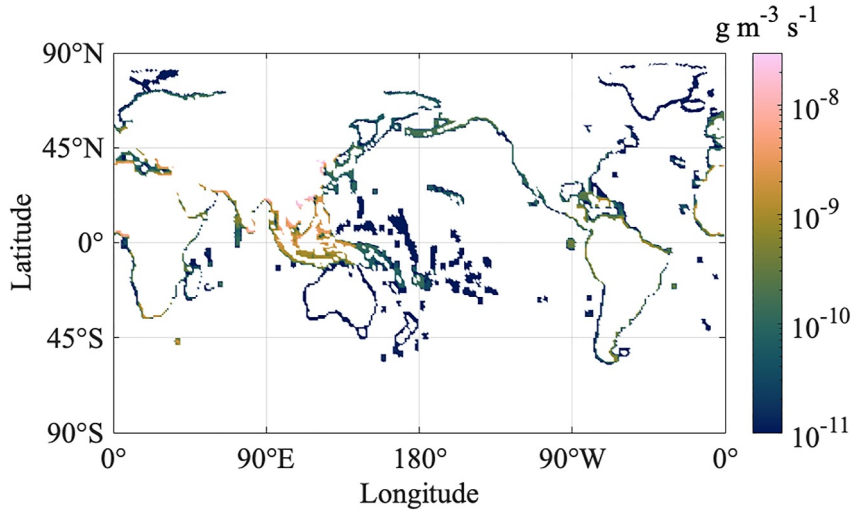



**Figure 1.** Map of the distribution and intensity of plastic release points [the $Q$ term in Equation 1] on the ECCO-LLC90 grid, based on the waste management report (Jambeck et al., 2015).

Consortium et al., 2021, 2023). Uniquely, the ECCOv4r4 is consistent not only with model equations (as is NEMO) but also with most available global-ocean observations through data assimilation. In contrast to an unconstrained model simulation such as NEMO, the ECCOv4r4 simulation has significantly smaller time-mean bias and drift relative to observations. These characteristics make the ECCO state estimates exceedingly well suited for studying passive tracers in the ocean.

The data assimilation is achieved using the ECCO modeling and estimation infrastructure, which includes the MITgcm as well as its automatically generated adjoint model (Wunsch & Heimbach, 2007). The ECCOv4r4 solution is based on a global, hydrostatic configuration of the MITgcm, integrated on the so-called ECCO-LLC90 grid, which has 1° nominal horizontal grid spacing with meridional refinement to 1/3° near the Equator, and a polar cap with ∼50 km grid spacing (Forget et al., 2015). There are 50 vertical levels with 10 m thickness near the surface, increasing to 450 m thickness at a maximum depth of 6 km, and the model time step is 1 hr. The adjoint-model-based ECCO optimization is able to compensate for model-measurement discrepancy via the adjustment of boundary conditions, for example, surface wind stress, and empirical model parameters such as the background diapycnal diffusivity (ECCO Consortium et al., 2021).

We take the ocean current velocity $\mathbf{u}$ and the diffusivity tensor $K$ from ECCOv4r4 as inputs to Equation 1. The velocity field $\mathbf{u}$ contains the resolved physics, for example, geostrophic and ageostrophic currents; while the diffusivity tensor $K$ represents unresolved physics and is calculated as the sum of diapycnal and along-isopycnal processes. The former includes the background and Gaspar-Gregoris-Lefevre components (Gaspar et al., 1990), and the latter is treated by the so-called GM-Redi parameterizations (Gent & McWilliams, 1990; Redi, 1982). Among these components, the space-dependent background and scalar magnitude of GM-Redi components are optimized through data assimilation, and the remaining parts are directly obtained from the modeled variables.

### 2.2. Buoyancy Advection Term

The buoyancy effect of particles is modeled by the term in advection form, $\partial_z(\tau w_r)$, in Equation 1. This is because a particle falling/rising with its terminal velocity $w_r$ is analogous to a particle being advected by an "external" velocity $w_r$. We note that this buoyancy advection term has to be in a mass-conservative form, in the sense that if there is no flux (or balanced flux) from the upper and lower boundary, the mass in the domain should stay constant. This property is satisfied only when the term is written as $\partial_z(\tau w_r)$ instead of $w_r\partial_z\tau$. In Mountford and Morales Maqueda (2019), the latter form is used at least judged from their presented equation, which may result in inconsistency in some of their results.

We now discuss the formula of $w_r$, dependent on both the particle size and density, as presented in Yang et al. (2014), Lobelle et al. (2021), and Dey et al. (2019). In particular, this formula has been used in a large eddy



21699291, 2025, 9, Downloaded from https://agupubs.onlinelibrary.wiley.com/doi/10.1029/2025JC023272 by University Of Michigan Library, Wiley Online Library on [30/08/2025]. See the Terms and Conditions (https://onlinelibrary.wiley.com/terms-and-conditions) on Wiley Online Library for rules of use; OA articles are governed by the applicable Creative Commons License

simulation (LES) model (Yang et al., 2014) to study the spread of oil plumes and in a 3D Lagrangian model (Lobelle et al., 2021) to study the time scale of vertical transport of particles. Dey et al. (2019) provide a thorough review on theories and experiments for particles subject to Stokes drag.

To start with, we consider a spherical particle with diameter $d$ at terminal velocity $w_r$, which is subject to the buoyancy force $B = g(\rho_w - \rho_p)(4\pi/3)(d/2)^3$ and the drag force $D = C_D(1/2)(\rho_w w_r^2)\pi(d/2)^2$. Balancing $B$ and $D$ leads to

$$w_r^2 C_D = \frac{4}{3} dg \frac{\rho_w - \rho_p}{\rho_w}, \tag{2}$$

where $g$ is the gravitational acceleration, $\rho_w$ is the water density, $\rho_p$ is the particle density, and $C_D$ is the drag coefficient that depends on the particle's shape and the particle Reynolds number $\mathrm{Re} \equiv \rho_w d w_r/\mu$, with $\mu$ being the dynamic viscosity of seawater. For typical size ($d < 0.1$ mm) and velocity ($w_r < 1$ mm s$^{-1}$) of MPs, we have $\mathrm{Re} = O(0.1) < 1$. Within this regime of Re, it has been shown that $C_D = 24/\mathrm{Re}$ irrespective of the shape of the particle (Dey et al., 2019). Therefore, the final formula can be written as

$$w_r = \frac{g(\rho_w - \rho_p) d^2}{18\mu}, \tag{3}$$

which we use in the simulation of Equation 1. As an example, consider biomaterial particles like phytodetritus, typically at mass density 1,388 kg m$^{-3}$ (Kooi et al., 2017). Equation 3 gives sinking velocities 494 μm s$^{-1}$ and 1978 μm s$^{-1}$ for particles at 50 μm and 100 μm, respectively, which are comparable to the measurement of at least 740 μm s$^{-1}$ in the marine snow event after the 2011 Tohoku-Oki Earthquake (although the size of particles in the measurement is not specified; Oguri et al., 2013). In addition, based on the buoyancy and drag forces to accelerate the particles, the typical time for an MP particle to reach terminal velocity is below 1 s (see Appendix A for a detailed analysis). As a result, the acceleration process can be safely neglected in our model with the total integration time of 26 years. We finally mention that for $\mathrm{Re} > 1$, the particle shape becomes relevant and modification to Equation 3 is needed, as discussed in Khatmullina and Isachenko (2017), although this will not be studied in the present paper.

### 2.3. Numerical and Case Setup

We numerically integrate Equation 1 with a finite volume method using the MITgcm "ptracers" package with additional implementation to include the buoyancy advection term (Tseng, 2025). The computation is performed on the ECCO-LLC90 grid with the same resolution and time step as chosen to generate the ECCOv4r4 data set. At all boundaries, a zero-flux boundary condition (including the flux due to $w_r$) is applied. The upper boundary is a free surface with its variability treated through a mapping technique presented in Adcroft and Campin (2004) and Campin et al. (2004). The $Q$ term in Equation 1 is handled by the "gchem" package, with positive values in g m$^{-3}$ s$^{-1}$ converted from the released trash weight and distributed in the surface cells along the coastlines (Figure 1). Sloped bathymetry is treated with partially filled cells in MITgcm (Adcroft et al., 1997).

We consider two idealistic cases and six realistic cases as summarized in Table 2, with the former providing insights on the particle behavior under extreme conditions and the latter aiming to understand the effect of particle properties on the distribution. The first idealistic case reduces the problem to 2D, which is an extreme case for particles with sufficiently high buoyancy ($w_r \to \infty$) so that they stay on the top layer near the free surface. This case is practically simulated by setting any vertical flux (including the ocean current and the buoyancy flux) and gradient to be zero in Equation 1 to avoid any downward transport. It can be hypothesized that the 2D idealistic case leads to higher particle concentration in gyres, since the particles accumulating in converging flow zones cannot be brought down away from the surface by downwelling as in 3D cases. The second idealized case is for neutrally buoyant particles to represent those with $d \to 0$ so that $w_r \to 0$. The six realistic cases are conducted for three types of plastics (PE for polyethylene, PS for polystyrene, and PVC for polyvinyl chloride) with densities lower than, comparable to, and higher than seawater, respectively. We further note that commonly used plastic materials typically have densities between 870 kg m$^{-3}$ and 1,420 kg m$^{-3}$, of which PE and PVC correspond to the lower and higher ends. For each particle density, two particle sizes are considered for their distinct



21699291, 2025, 9, Downloaded from https://agupubs.onlinelibrary.wiley.com/doi/10.1029/2025JC023272 by University Of Michigan Library, Wiley Online Library on [30/08/2025]. See the Terms and Conditions (https://onlinelibrary.wiley.com/terms-and-conditions) on Wiley Online Library for rules of use; OA articles are governed by the applicable Creative Commons License

**Table 2**
*Summary of Particle Properties in the Two Idealistic and Six Realistic Cases*

| Particle label | Mass density (kg m$^{-3}$) | Diameter (μm) | $w_r$ (μm s$^{-1}$) |
|---|---|---|---|
| 2D surface | NA | NA | NA |
| Neutrally buoyant | NA | NA | 0 |
| PE-10 | 900 | 10 | 6.3 |
| PE-1 | 900 | 1 | 0.06 |
| PS-100 | 1,030 | 100 | −27.3 |
| PS-10 | 1,030 | 10 | −0.27 |
| PVC-10 | 1,200 | 10 | −9.5 |
| PVC-1 | 1,200 | 1 | −0.09 |

*Note*. A typical value of terminal velocity is estimated based on a seawater density $\rho_w = 1025$ kg m$^{-3}$. Typical vertical ocean current has magnitude around 5 μm s$^{-1}$.

behaviors in the stationary distribution. In particular, for PS, we consider sizes of 100 μm and 10 μm, while for PE and PVC, we consider 10 μm and 1 μm. These choices of sizes are made such that for each material, we have one size smaller than the critical value for the particles to behave as neutrally buoyant tracers and the other greater for them to behave completely differently.

## 3. Results

### 3.1. Idealistic Cases

The idealized case for 2D surface particles reproduces accumulation patterns in the five subtropical gyres at North Pacific, South Pacific, North Atlantic, South Atlantic, and Indian Ocean found in previous works (Figure 2; Figure B1; Chenillat et al., 2021; Lebreton et al., 2012; Maximenko et al., 2012; van Sebille et al., 2012). In addition, we observe another accumulation in the Arctic area, which is also present in the 3D Eulerian model for positively buoyant particles (see Figure 3 of Mountford and Morales Maqueda (2019)). This accumulation zone is not recognized in previous Lagrangian or statistical studies because the ocean current data obtained by GDP does not adequately cover the Arctic area.

In the idealized case for 3D neutrally buoyant particles, the gyre accumulation pattern is much weaker compared to the 2D result, with some weak accumulations present in North Pacific, North Atlantic, South Atlantic, and Indian Ocean, but not South Pacific (Figure 3a). Vertically, the particles penetrate downward up to about 1 km depth, which is much deeper than the MLD of about 200 m (Figure 3b). We have checked that the penetration depth has not reached a stationary state at the end of the 26-year simulation. This is likely due to the ubiquitous diapycnal mixing in the ocean interior, which tends to move particles downward continuously through the mixing process. A graphical comparison of this result to that in Mountford and Morales Maqueda (2019) is also provided in Appendix B (Figure B2). We will use the distribution of neutrally buoyant particles (Figure 3) as a reference to understand that of realistic particles with sufficiently small size in the following discussions.

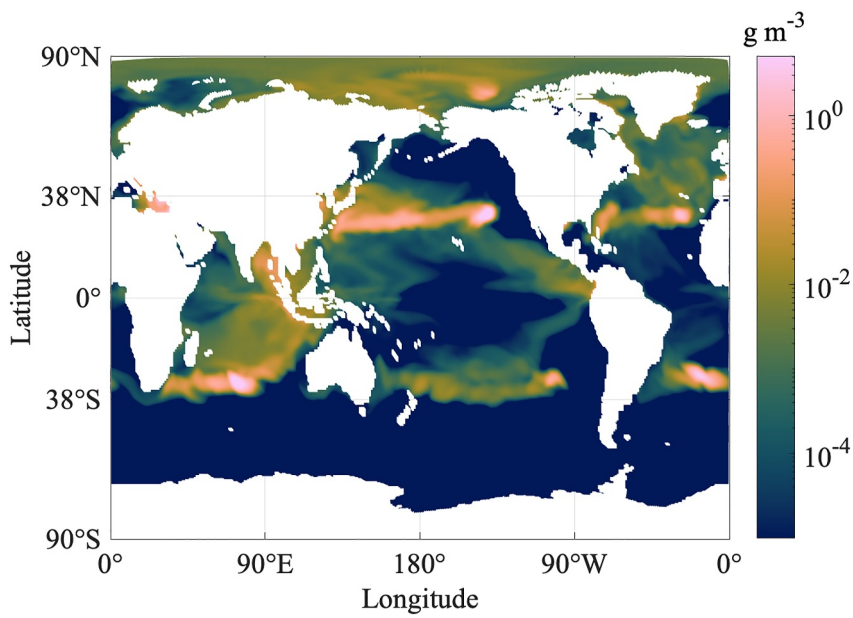



**Figure 2.** Surface particle concentration in the 2D idealistic case, averaged over the last year of the 26-year simulation.



21699291, 2025, 9, Downloaded from https://agupubs.onlinelibrary.wiley.com/doi/10.1029/2025JC023272 by University Of Michigan Library, Wiley Online Library on [30/08/2025]. See the Terms and Conditions (https://onlinelibrary.wiley.com/terms-and-conditions) on Wiley Online Library for rules of use; OA articles are governed by the applicable Creative Commons License

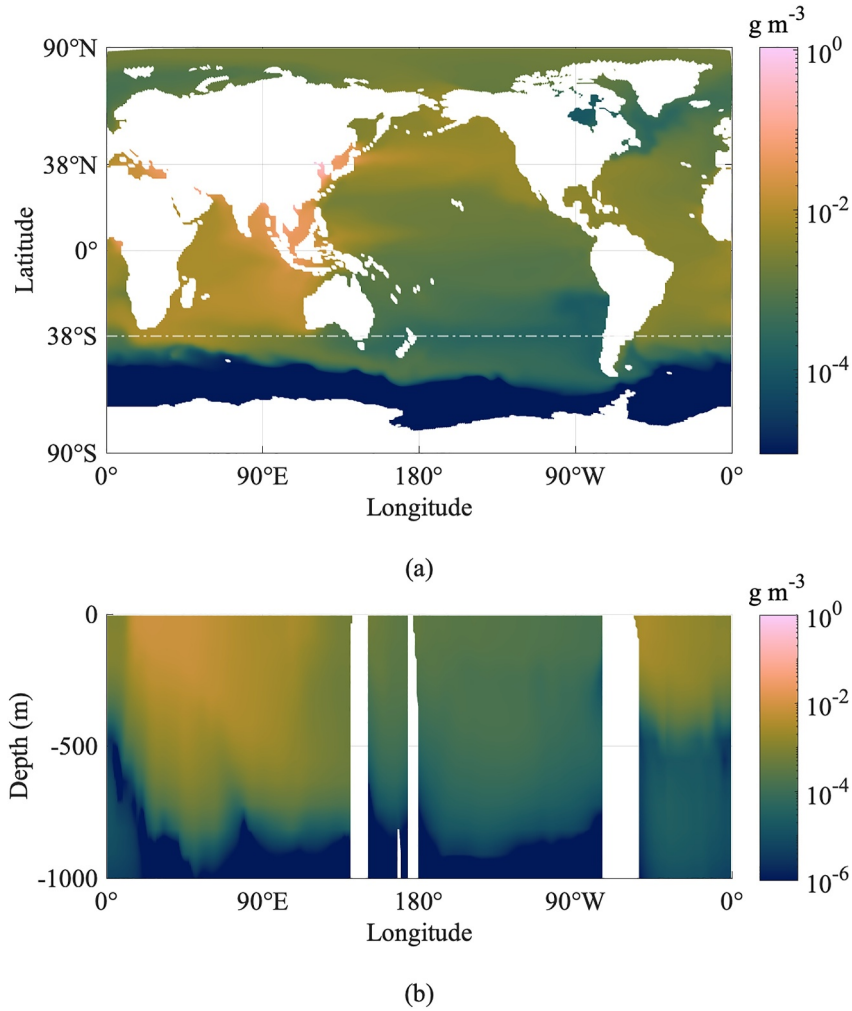



**Figure 3.** Concentration of neutrally buoyant particles, averaged over the last year of the 26-year simulation and plotted (a) on the surface and (b) over a vertical slice at 38°S and upper 1 km of the ocean. A dash-dotted line denoting 38°S is included in (a).

### 3.2. Realistic Cases

#### 3.2.1. Low-Density Particles

Polyethylene (PE) is a plastic material with density lower than that of seawater. Here, we take a representative density of 900 kg $m^{-3}$ and two particle sizes of 10 μm (PE-10) and 1 μm (PE-1). The horizontal and vertical concentrations averaged over the final year of 26-year simulations for both particle sizes are shown in Figure 4.

For PE-10 (i.e., the larger particles), we see a clear accumulation of particles in the five gyres identified in the 2D results, but with weaker concentration in the Arctic ocean (Figures 2 and 4a, note that different color bars are used). As expected, the concentrations near the gyres' centers are generally lower than those predicted by the 2D case due to the vertical downwelling motion. The majority of PE-10 particles stay close to the sea surface within the upper 200 m, that is, the MLD, except in the Indian Ocean gyre where MPs penetrate downward to 600 m depth (Figure 4c) due to the stronger downwelling there. For PE-1 (i.e., the smaller particles with a critical size of 1 μm), in contrast, the accumulation within gyres becomes weaker, and there are little differences between its concentrations and those of neutrally buoyant particles (Figures 3, 4b, and 4d). This is because the terminal velocity at 0.06 μm $s^{-1}$, which at most results in 50 m upward shift of the particles in the 26 years of evolution, is too weak to influence a particle's vertical motion.



21699291, 2025, 9, Downloaded from https://agupubs.onlinelibrary.wiley.com/doi/10.1029/2025JC023272 by University Of Michigan Library, Wiley Online Library on [30/08/2025]. See the Terms and Conditions (https://onlinelibrary.wiley.com/terms-and-conditions) on Wiley Online Library for rules of use; OA articles are governed by the applicable Creative Commons License

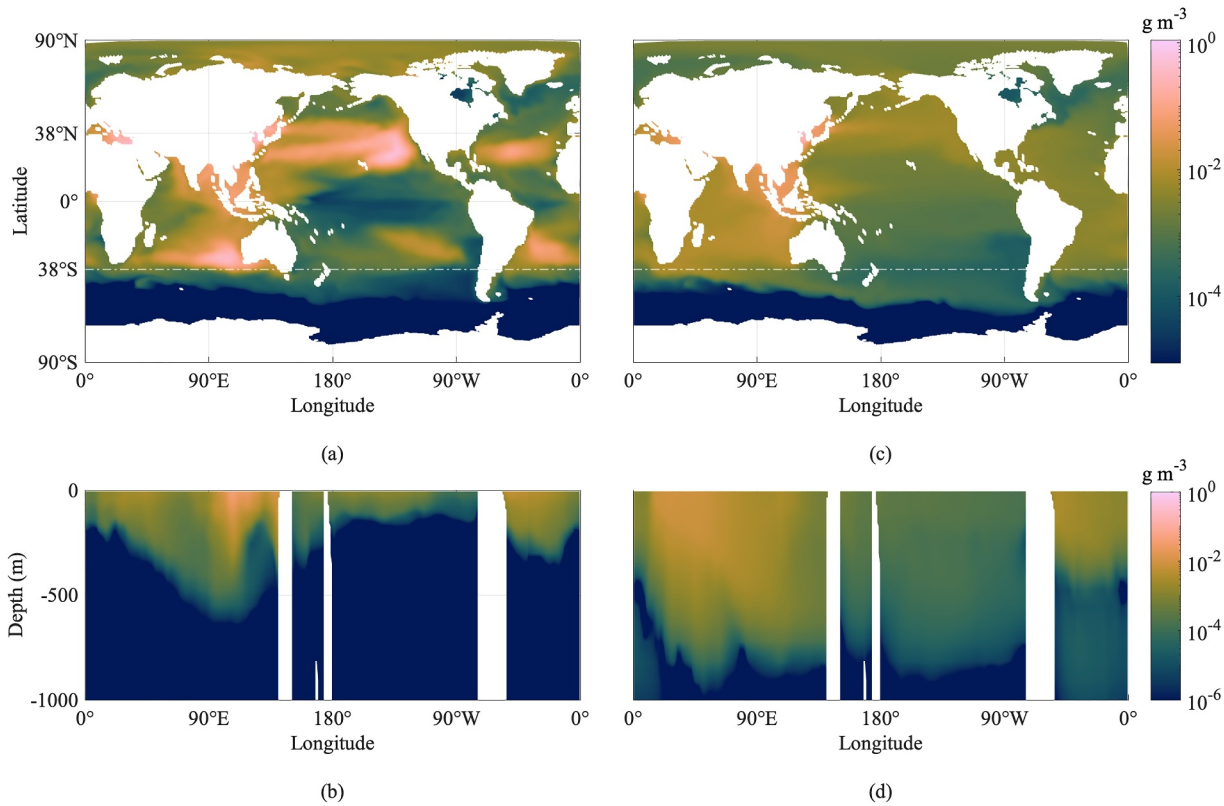



**Figure 4.** Distribution of PE particles of two sizes, averaged over the last year of the 26-year simulation. The concentration of PE-10 is shown (a) on the surface and (c) over a vertical slices at 38°S, and the counterparts for PE-1 are shown in (b, d). A dash-dotted line denoting 38°S is included in (a, c).

Comparing results regarding PE-10 and PE-1, we find that larger particles are more likely to accumulate in the gyres close to the surface. Therefore, near the sea surface, it should be expected that most particles with a similar density as PE have sizes above a threshold ($d \gtrsim 10$ μm), while smaller particles are "sifted" downward by the vertical mixing process.

### 3.2.2. Particles With Density Close to Seawater

Polystyrene (PS) is a plastic material with a density comparable to that of seawater. We consider a representative density of 1,030 kg m$^{-3}$, and two sizes of 10 μm (PS-10) and 100 μm (PS-100). The PS-100 particles are mostly concentrated at a depth of about 650 m where the local seawater density matches the particle density (Figure 5c). This is the neutrally buoyant depth for PS-100 particles, and any deviation from this depth tends to be corrected by buoyancy, which acts as a restoring force. The particle concentration at 650 m depth is high in coastal regions due to fast sinking of the particles once released from the coastline (Figure 5a). As they reach about 650 m depth, the horizontal advection almost vanishes due to the slow horizontal ocean flow motion at that depth. Therefore, there exists a sinking time scale $T_s \approx 9$ months determined as the time it takes for a particle to sink to the stationary layer, beyond which the particles are not further advected to the open ocean.

For the PS-10 particles, in contrast, the distribution becomes similar to that of the neutrally buoyant particles (Figures 3, 5b, and 5d). We note that for density of 1,030 kg m$^{-3}$, 10 μm is demonstrated to be the critical size for the neutrally buoyant behavior to occur, whereas for PE (density being 900 kg m$^{-3}$, discussed in §3.2.1), the critical size goes down to 1 μm. This can be understood from Equation 3, where $w_r$ can be made sufficiently small by either a small particle size $d$ or small density difference $\rho_w - \rho_p$. In addition, only small PS particles are expected to be found near the ocean surface, in contrast to the PE particles.



21699291, 2025, 9, Downloaded from https://agupubs.onlinelibrary.wiley.com/doi/10.1029/2025JC023272 by University Of Michigan Library, Wiley Online Library on [30/08/2025]. See the Terms and Conditions (https://onlinelibrary.wiley.com/terms-and-conditions) on Wiley Online Library for rules of use; OA articles are governed by the applicable Creative Commons License

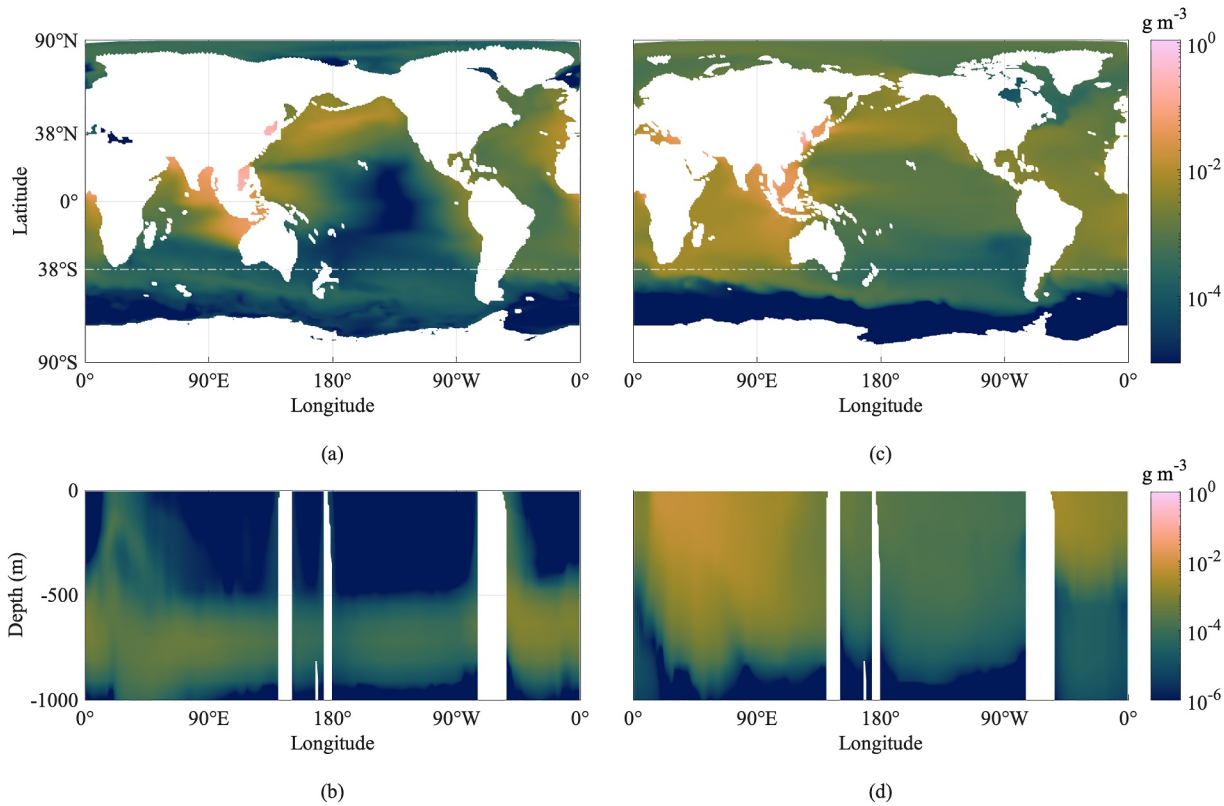



**Figure 5.** Distribution of PS particles of two sizes, averaged over the last year of the 26-year simulation. The concentration of PS-100 is plotted (a) horizontally at 650 m depth and (c) over a vertical slices at 38°S. The concentration of PS-10 is shown (b) on the surface and (d) over vertical slices at 38°S. A dash-dotted line denoting 38°S is included in (a, c).

### 3.2.3. High-Density Particles

Polyvinyl chloride (PVC) is a high-density plastic material, in our model with a representative density of 1,200 kg $m^{-3}$, which is higher than seawater density typically in the range of $1000 < \rho_w < 1050$ kg $m^{-3}$. Simulation results for two particle sizes, 10 μm (PVC-10) and 1 μm (PVC-1), are shown in Figure 6.

At the end of the 26-year simulation, most PVC-10 particles sink to the sea bottom and accumulate in the ocean trenches, with higher concentration near the coastline (Figure 6a). However, there are some signatures of particles present at all depths, originating from particles released from the coastline and in their process to sink to the bottom (Figure 6c). We note that for PVC-10, the time scale of a particle with $w_r \approx -9.5$ μm $s^{-1}$ sinking from the surface to the bottom of 6 km is about 20 years. This value of $T_s$ is comparable with the duration of our simulations, which yields sufficient time for particles to spread horizontally before sinking to the bottom.

The distribution of PVC-1 particles again becomes similar to that of neutrally buoyant particles (Figures 6b and 6d). At a terminal vertical velocity of only $w_r \approx -0.09$ μm $s^{-1}$, 1 μm is the critical size for PVC particles to exhibit neutrally buoyant behavior. As a result, only small PVC particles are expected to be present near the ocean surface, similar to PS particles.

### 3.3. Seasonal Variation of Surface Concentration

Seasonal variations in the concentration of particles have been recorded using a numerical approach (Mountford & Morales Maqueda, 2019) and later revealed in remote sensing data from CYGNSS (Evans & Ruf, 2022). In our study and discussions regarding seasonal variations, we focus on the surface concentration of PE-10 particles, which shows the highest concentration at sea surface among all particles. As an example, Figure 7 shows a 5-year time series of PE-10 surface concentration averaged over the North Pacific Ocean, where the seasonal pattern is evident.



21699291, 2025, 9, Downloaded from https://agupubs.onlinelibrary.wiley.com/doi/10.1029/2025JC023272 by University Of Michigan Library, Wiley Online Library on [30/08/2025]. See the Terms and Conditions (https://onlinelibrary.wiley.com/terms-and-conditions) on Wiley Online Library for rules of use; OA articles are governed by the applicable Creative Commons License

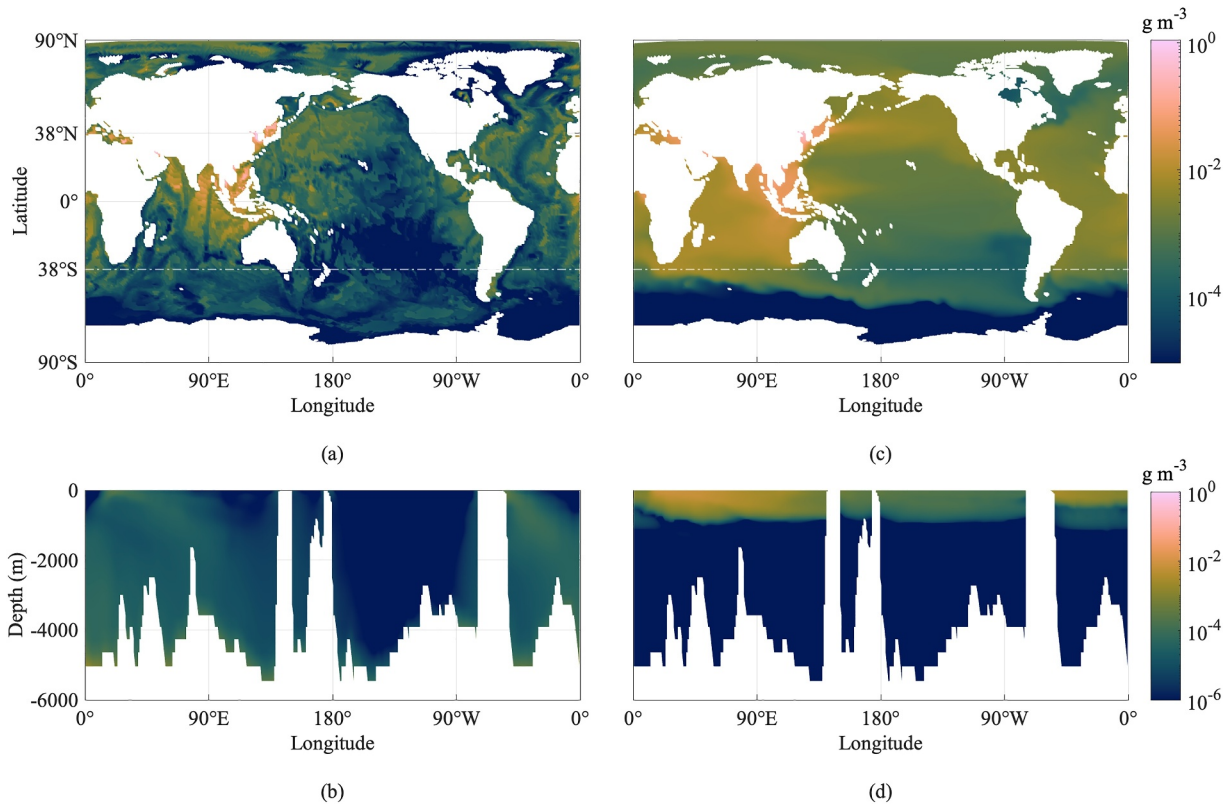



**Figure 6.** Distribution of PVC particles of two sizes, averaged over the last year of the 26-year simulation. The concentration of PVC-10 is shown (a) at the ocean bottom and (c) over a vertical slice at 38°S covering all ocean depths. The concentration of PVC-1 is shown (b) on the surface with a dash-dotted line on 38°S and (d) over a vertical slice at 38°S covering only the upper 1 km. A dash-dotted line denoting 38°S is included in (a, c).

We perform a comparison between our model output and CYGNSS observation in terms of the phase of the seasonal cycle. For this purpose, we define the peak time, $T_p$, as the month within the year 2017 when a maximum value of concentration of MPs is recorded on the ocean surface. In particular, the $T_p$ of CYGNSS is derived from the CYGNSS Level 3 ocean microplastic concentration version 1.0 data record at $1/4°$ resolution. Consistent with CYGNSS, the modeled concentration peaks in summer in both the Northern and Southern hemispheres (see Figures 8a and 8b for a visual comparison). To provide a quantitative measure of the agreement, we define

$$\Delta T_p = \begin{cases} T_{p,\mathrm{CYGNSS}} - T_{p,\mathrm{MODEL}} + 12, & \text{if } T_{p,\mathrm{CYGNSS}} - T_{p,\mathrm{MODEL}} < -6, \\ T_{p,\mathrm{CYGNSS}} - T_{p,\mathrm{MODEL}} - 12, & \text{if } T_{p,\mathrm{CYGNSS}} - T_{p,\mathrm{MODEL}} > 6, \\ T_{p,\mathrm{CYGNSS}} - T_{p,\mathrm{MODEL}}, & \text{otherwise.} \end{cases} \tag{4}$$

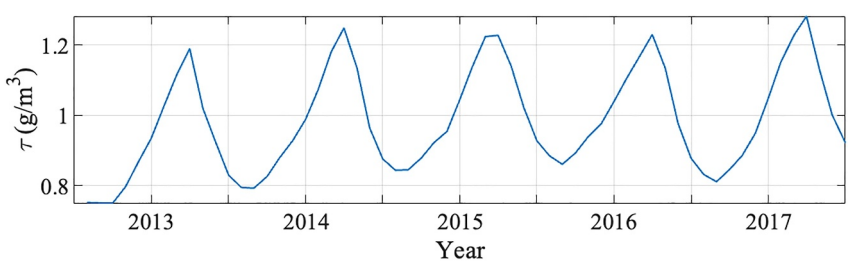



**Figure 7.** Spatially averaged surface concentration of PE-10 MPs over the North Pacific [20°N–35°N, 130°W–150°E] across 5 years.



21699291, 2025, 9, Downloaded from https://agupubs.onlinelibrary.wiley.com/doi/10.1029/2025JC023272 by University Of Michigan Library, Wiley Online Library on [30/08/2025]. See the Terms and Conditions (https://onlinelibrary.wiley.com/terms-and-conditions) on Wiley Online Library for rules of use; OA articles are governed by the applicable Creative Commons License

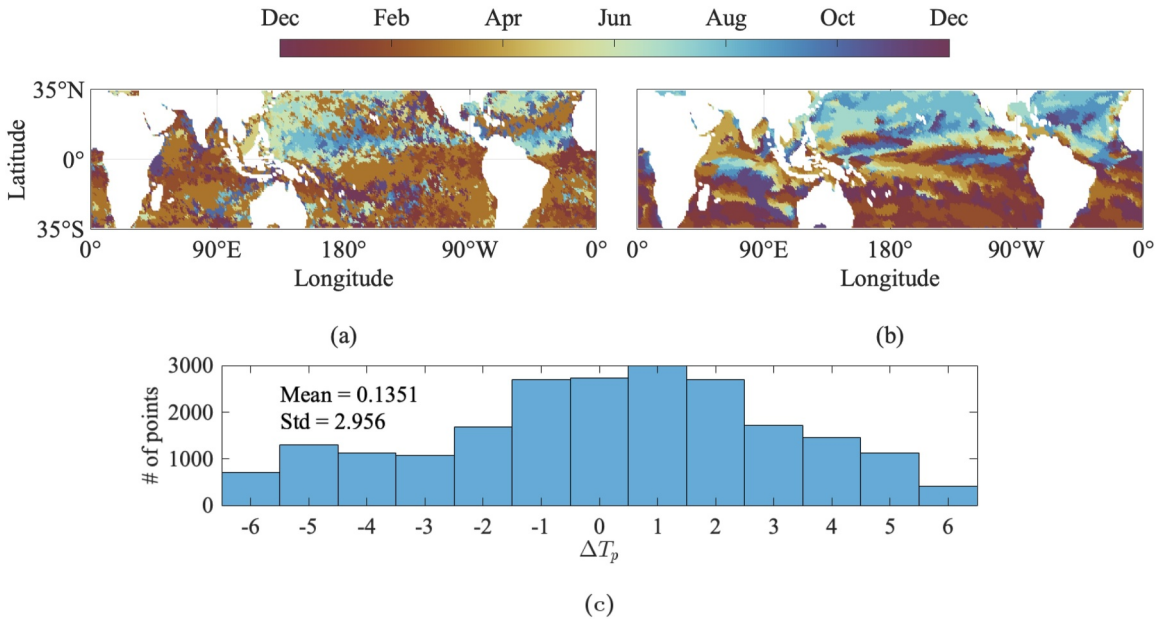



**Figure 8.** Map of $T_p$ from (a) CYGNSS observation and (b) the PE-10 model result; and (c) the statistics of $\Delta T_p$, which represents the difference between (a, b), as defined in (4).

The three-branch function in Equation 4 accounts for the cyclic nature of $T_p$, and it ensures that $\Delta T_p$ is bounded by $[-6, 6]$. We plot the statistics of $\Delta T_p$ in Figure 8c, which shows that most data (quantitatively, 72% of them) fall within $\pm 3$ months. Considering many uncertainties in the observation, this should be viewed as a reasonable agreement. For example, CYGNSS retrieves the concentration of MPs from the surface roughness, which is dominantly affected by surfactants (Sun et al., 2023), as well as precipitation and sea surface air pressure.

To study the physical mechanism of the seasonal variation, we inspect three candidate quantities that may be related to the seasonal variation of surface concentration. The first one is the horizontal divergence of the surface water, $\nabla_h \cdot \mathbf{u}_h$, which is correlated with particle transport within the gyre (Mensa et al., 2015). The second one is

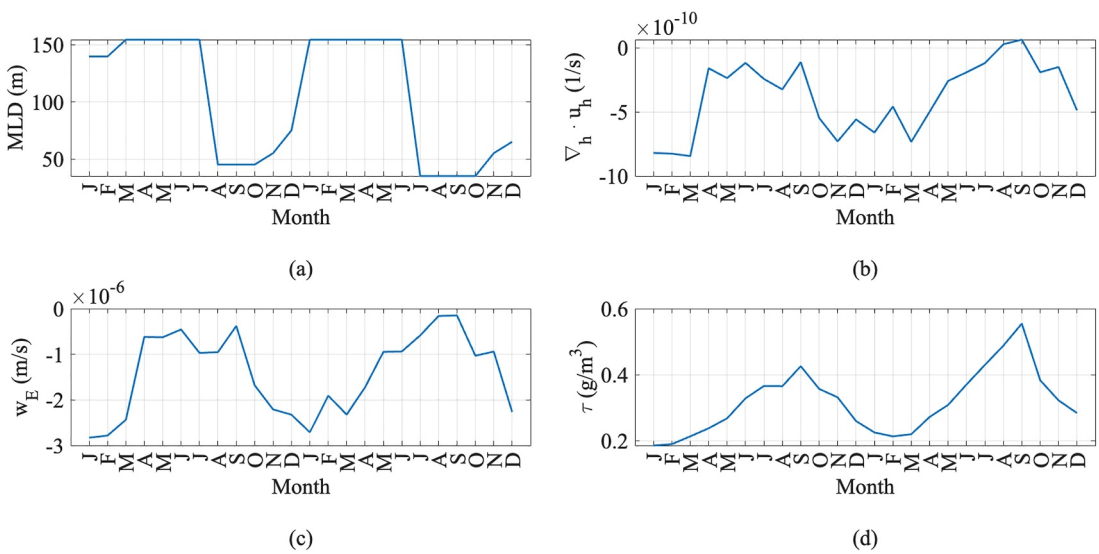



**Figure 9.** Two-year time series of (a) the MLD, (b) $\nabla_h \cdot \mathbf{u}_h$ the horizontal divergence of ocean currents, (c) $w_E$ the Ekman upwelling velocity, and (d) $\tau$ the surface concentration of MPs, all taken at [30°N, 130°W] in the North Pacific gyre.



21699291, 2025, 9, Downloaded from https://agupubs.onlinelibrary.wiley.com/doi/10.1029/2025JC023272 by University Of Michigan Library, Wiley Online Library on [30/08/2025]. See the Terms and Conditions (https://onlinelibrary.wiley.com/terms-and-conditions) on Wiley Online Library for rules of use; OA articles are governed by the applicable Creative Commons License

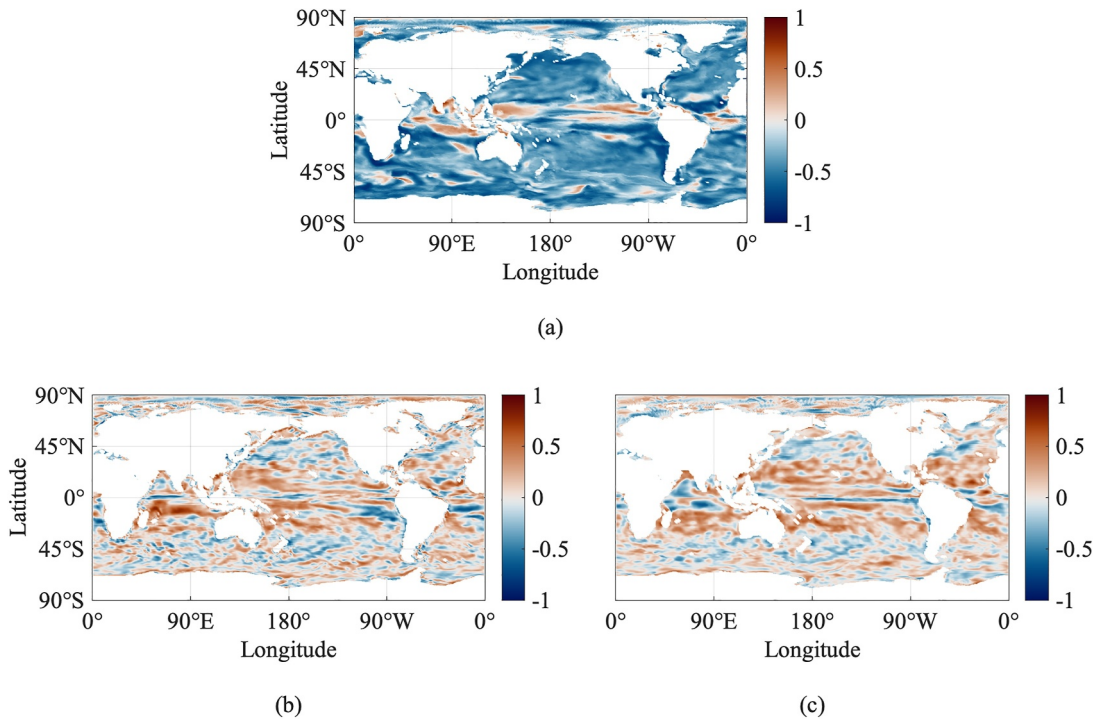



**Figure 10.** Maps of correlation coefficients computed over 6 years (2012–2017) between the surface concentration $\tau$ and (a) the MLD, (b) the horizontal divergence of surface current $\nabla_h \cdot \mathbf{u}_h$, and (c) the Ekman upwelling velocity $w_E$.

the Ekman upwelling velocity, $w_E$, which moves particles toward the surface, therefore changes the amount of particles near the surface. The Ekman velocity is computed from the wind stress curl (as part of the state estimate in ECCOv4r4). The third one is the MLD, affecting the vertical distribution of positively buoyant particles near the surface. It is shown by Richon et al. (2022) that the surface concentration varies seasonally due to the vertical transport of particles, based on which a hypothesis is made that MLD is a relevant parameter. In practice, we compute MLD as the depth where the buoyancy frequency is maximized (Carvalho et al., 2017).

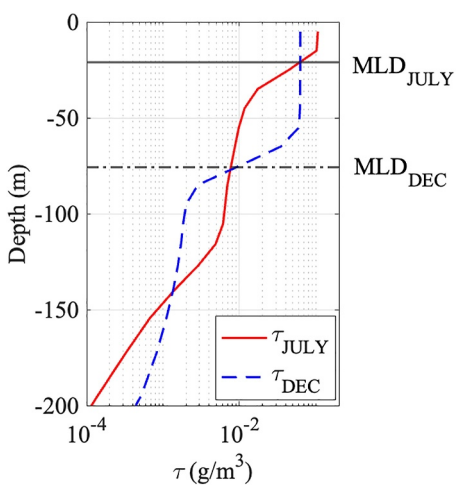



**Figure 11.** Vertical profile of the PE-10 plastic distribution taken at [30°N, 130°W] in July 2017 (red) and December 2017 (blue). The mixed layer depths are indicated in July by solid black lines and in December by dashed black lines.

In Figure 9, we show the 2-year time series of the surface PE-10 concentration and the three candidate quantities, which are taken at [30°N, 130°W] within the North Pacific gyre. The seasonal patterns in all these quantities are clear from the figure. To understand which candidate quantity is most relevant to the seasonal variation of $\tau$, we map globally the correlation coefficient between surface $\tau$ and each of the three quantities in Figure 10. With correlation coefficients close to $-1$ globally (Figure 10a), MLD is shown to be the most correlated factor. In contrast, $\nabla_h \cdot \mathbf{u}_h$ and $w_E$ (Figures 10b and 10c) have much weaker correlations, ruling out their physical influences on seasonal variations of $\tau$, although the two quantities may be relevant to the formation of stationary patches.

The correlation between $\tau$ and the MLD can be understood from a homogeneously mixed water column within the ML. Positively buoyant particles such as PE-10 are well mixed in the ML and diminish rapidly below. This is demonstrated well in Figure 11, where different vertical profiles of particle concentration at [30°N, 130°W] are shown in July and December (with the main features also valid in other months of the year and other locations). Since most PE-10 particles consistently locate within the ML (due to sufficient buoyancy), their mass in the layer is almost conserved. Furthermore, because of the uniform vertical particle concentration in the ML, the particle concentration scales inversely with the MLD, leading to the observed correlation.



21699291, 2025, 9, Downloaded from https://agupubs.onlinelibrary.wiley.com/doi/10.1029/2025JC023272 by University Of Michigan Library, Wiley Online Library on [30/08/2025]. See the Terms and Conditions (https://onlinelibrary.wiley.com/terms-and-conditions) on Wiley Online Library for rules of use; OA articles are governed by the applicable Creative Commons License

## 4. Conclusion and Discussion

We develop a 3D Eulerian model to study the distribution of MPs in the global ocean, where the buoyancy effect of the plastic particles with various densities and sizes is incorporated through a terminal velocity convection term formulated in a mass-conservative way. The effect of particle size on the resulting distribution is studied for the first time in this paper. Among the six representative types of particles studied, only low-density particles with sufficient size (e.g., PE with diameter $d = 10$ μm) accumulate in the five subtropical gyres, forming the garbage patches in agreement with previous modeling studies and satellite observations. The aggregation of PS-100 particles in ocean interior suggests that plastic materials like polystyrene (PS) have a larger impact on the mesopelagic ecosystems than low-density materials. For all plastic materials studied, as the particle size decreases below a threshold ($\lesssim$1 μm for PE and PVC, $\lesssim$10 μm for PS), their distribution converges to that of neutrally buoyant particles, exhibiting weaker accumulation on the surface with a deeper penetration into the ocean interior of approximately 1 km. In addition, we study the seasonal variation of surface concentration of positively buoyant particles (PE-10), which resembles CYGNSS observations in its covered area in terms of the phase of the seasonal cycle. We further find that this seasonal variation correlates well with that of the MLD, based on which a physical explanation is established: Within the ML, a conserved amount of particles is uniformly distributed, whose concentration thus changes with the MLD.

We conclude by remarking again that our model takes consideration of particle sizes, which is an important improvement over earlier models and allows many potential future developments. Processes that change the particles' size over time, for example, fragmentation and biofouling, can only be built upon and resolved by such a model. As our current and future work, we will implement fragmentation and biofouling processes in our Eulerian model framework by augmenting the state space to include particle size. We also plan to develop a data assimilation interface that incorporates remote-sensing data (e.g., CYGNSS) and field measurements into the model. Our envisaged future model will be a data-assimilated model incorporating a spectrum of different particle properties (size and density) as well as property-changing processes such as fragmentation and biofouling.

## Appendix A: Time Scale to Reach the Terminal Velocity

Consider a round particle moving at an instantaneous velocity $w$, subject to a buoyancy force $B = g(\rho_w - \rho_p)(4\pi/3)(d/2)^3$ and a drag force $D = (12/\mathrm{Re})(\rho_w w^2)\pi(d/2)^2$. Force balance acting on the particle leads to

$$\rho_p \frac{4\pi}{3}\left(\frac{d}{2}\right)^3 \frac{dw}{dt} = g(\rho_w - \rho_p)\,\frac{4\pi}{3}\left(\frac{d}{2}\right)^3 - \frac{12\mu w}{d}\pi\left(\frac{d}{2}\right)^2. \tag{A1}$$

This forms an ODE for $w$

$$\frac{dw}{dt} = -\frac{18\mu}{\rho_p d^2} \times w + \frac{g(\rho_w - \rho_p)}{\rho_p}. \tag{A2}$$

Substituting Equation 3 into Equation A2 gives

$$\frac{dw}{dt} = \frac{18\mu}{\rho_p d^2} \times (w - w_r). \tag{A3}$$

Let $\Delta w(t) = w(t) - w_r$, this yields a solution

$$\Delta w(t) = \Delta w(0) \times \exp\left\{-\frac{18\mu}{\rho_p d^2} t\right\}. \tag{A4}$$

That is, given any difference between the instantaneous velocity and the terminal velocity of a particle, the difference decreases exponentially in time. From the exponent in Equation A4, the $e$-folding time scale $T_e$ for this velocity difference is



21699291, 2025, 9, Downloaded from https://agupubs.onlinelibrary.wiley.com/doi/10.1029/2025JC023272 by University Of Michigan Library, Wiley Online Library on [30/08/2025]. See the Terms and Conditions (https://onlinelibrary.wiley.com/terms-and-conditions) on Wiley Online Library for rules of use; OA articles are governed by the applicable Creative Commons License

$$T_e = \frac{\rho_p d^2}{18\mu}. \tag{A5}$$

For $\rho_p \sim 1000$ kg m$^{-3}$ and $\mu = 0.001$ Pa s, Equation A5 gives $T_e = 0.05$ s even for large particles of diameter $d = 1$ mm.

## Appendix B: Graphical Comparison With Earlier Studies

In this appendix, we present comparisons of our results in the idealistic cases to earlier relevant studies. Figure B1 shows a comparison of the result in our 2D idealistic case to that in Chenillat et al. (2021), Lebreton et al. (2012), Maximenko et al. (2012), and van Sebille et al. (2012). Figure B2 shows a comparison of the result in our neutrally buoyant case to that in Mountford and Morales Maqueda (2019) with the same color bar.

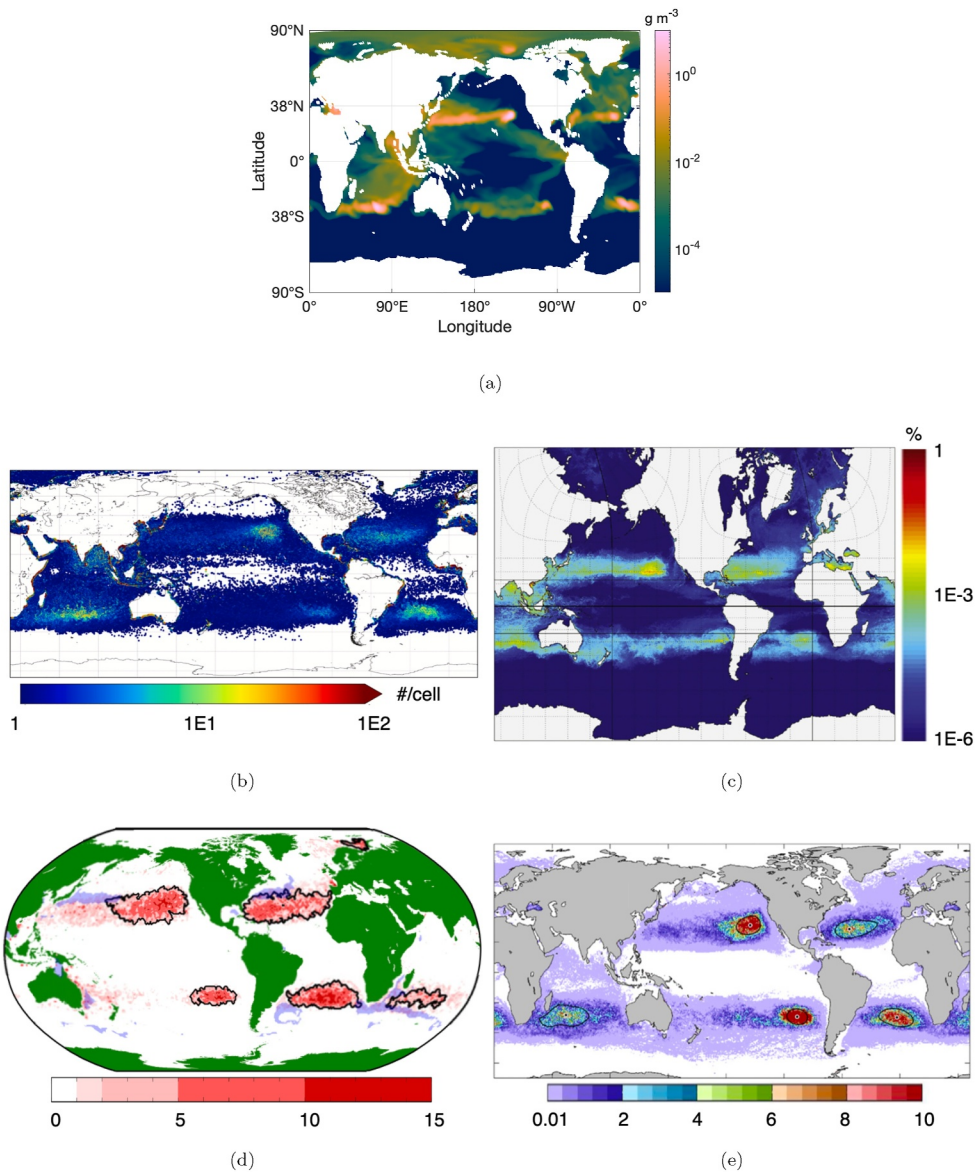



**Figure B1.** (a) Copy of Figure 2, (b) particle number density ( per $1/12° \times 1/12°$ cell) taken from Chenillat et al. (2021), (c) particle concentration (unit unspecified) taken from Lebreton et al. (2012), (d) tracer amplification factor taken from (van Sebille et al. (2012), (e) particle concentration (unit unspecified) obtained by Maximenko et al. (2012).



21699291, 2025, 9, Downloaded from https://agupubs.onlinelibrary.wiley.com/doi/10.1029/2025JC023272 by University Of Michigan Library, Wiley Online Library on [30/08/2025]. See the Terms and Conditions (https://onlinelibrary.wiley.com/terms-and-conditions) on Wiley Online Library for rules of use; OA articles are governed by the applicable Creative Commons License

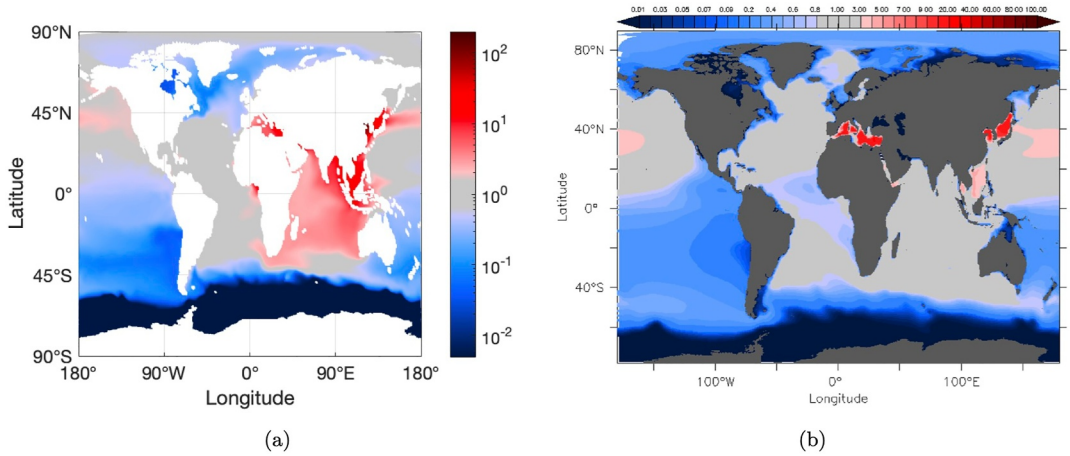



**Figure B2.** Neutrally buoyant particle surface distribution, normalized with global mean values, obtained by (a) our model and (b) Mountford and Morales Maqueda (2019) with the same color bar.

## Data Availability Statement

To reproduce simulations in this paper, one can follow five procedures briefly summarized below.

1. Download the MITgcm package.
2. Download the ECCOv4r4 data set (in particular, the forcing and initial conditions for MITgcm to reproduce the ECCOv4r4 data set).
3. Download the additional code (used in step 4) and inputs (used in step 5) at https://zenodo.org/records/16903982 (Tseng, 2025) to treat additional terms in Equation 1. Animations of some simulation results are also provided in the repository.
4. Compile both the original MITgcm code and additional code in Step 3.
5. Conduct simulations with different inputs on particle properties.

A file uploaded at https://github.com/zizien1019/reproduce_eccov4r4_online_68o/blob/main/Read_me.pdf contains much more detailed step-by-step instructions.

**Acknowledgments**
This research was supported in part by NASA Science Mission Directorate contract 80LARC21DA003 with the University of Michigan.

## References

Adcroft, A., & Campin, J.-M. (2004). Rescaled height coordinates for accurate representation of free-surface flows in ocean circulation models. *Ocean Modelling*, *7*(3–4), 269–284. https://doi.org/10.1016/j.ocemod.2003.09.003

Adcroft, A., Hill, C., & Marshall, J. (1997). Representation of topography by shaved cells in a height coordinate ocean model. *Monthly Weather Review*, *125*(9), 2293–2315. https://doi.org/10.1175/1520-0493(1997)125<2293:rotbsc>2.0.co;2

Borrelle, S. B., Ringma, J., Law, K. L., Monnahan, C. C., Lebreton, L., McGivern, A., et al. (2020). Predicted growth in plastic waste exceeds efforts to mitigate plastic pollution. *Science*, *369*(6510), 1515–1518. https://doi.org/10.1126/science.aba3656

Campin, J.-M., Adcroft, A., Hill, C., & Marshall, J. (2004). Conservation of properties in a free-surface model. *Ocean Modelling*, *6*(3–4), 221–244. https://doi.org/10.1016/s1463-5003(03)00009-x

Carvalho, F., Kohut, J., Oliver, M. J., & Schofield, O. (2017). Defining the ecologically relevant mixed-layer depth for Antarctica's coastal seas. *Geophysical Research Letters*, *44*(1), 338–345. https://doi.org/10.1002/2016gl071205

Chenillat, F., Huck, T., Maes, C., Grima, N., & Blanke, B. (2021). Fate of floating plastic debris released along the coasts in a global ocean model. *Marine Pollution Bulletin*, *165*, 112116. https://doi.org/10.1016/j.marpolbul.2021.112116

Cózar, A., Echevarría, F., González-Gordillo, J. I., Irigoien, X., Úbeda, B., Hernández-León, S., et al. (2014). Plastic debris in the open ocean. *Proceedings of the National Academy of Sciences of the United States of America*, *111*(28), 10239–10244. https://doi.org/10.1073/pnas.1314705111

Dey, S., Zeeshan Ali, S., & Padhi, E. (2019). Terminal fall velocity: The legacy of Stokes from the perspective of fluvial hydraulics. *Proceedings of the Royal Society A: Mathematical, Physical and Engineering Sciences*, *475*(2228), 20190277. https://doi.org/10.1098/rspa.2019.0277

ECCO Consortium, Fukumori, I., Wang, O., Fenty, Heimbach, P., & Ponte, R. M. (2021). *Synopsis of the ECCO central production global ocean and sea-ice state estimate, version 4 release 4*. Zenodo. https://doi.org/10.5281/zenodo.4533349

ECCO Consortium, Fukumori, I., Wang, O., Fenty, Heimbach, P., & Ponte, R. M. (2023). ECCO central estimate (version 4 release 4). Retrieved from https://ecco.jpl.nasa.gov/drive/files/Version4/Release4

Eriksen, M., Lebreton, L. C. M., Carson, H. S., Thiel, M., Moore, C. J., Borerro, J. C., et al. (2014). Plastic pollution in the world's oceans: More than 5 trillion plastic pieces weighing over 250,000 tons afloat at sea. *PLoS One*, *9*(12), e111913. https://doi.org/10.1371/journal.pone.0111913

Evans, M. C., & Ruf, C. S. (2022). Toward the detection and imaging of ocean microplastics with a spaceborne radar. *IEEE Transactions on Geoscience and Remote Sensing*, *60*, 1–9. https://doi.org/10.1109/TGRS.2021.3081691



21699291, 2025, 9, Downloaded from https://agupubs.onlinelibrary.wiley.com/doi/10.1029/2025JC023272 by University Of Michigan Library, Wiley Online Library on [30/08/2025]. See the Terms and Conditions (https://onlinelibrary.wiley.com/terms-and-conditions) on Wiley Online Library for rules of use; OA articles are governed by the applicable Creative Commons License

Forget, G., Campin, J.-M., Heimbach, P., Hill, C. N., Ponte, R. M., & Wunsch, C. (2015). Ecco version 4: An integrated framework for non-linear inverse modeling and global ocean state estimation. *Geoscientific Model Development*, *8*(10), 3071–3104. https://doi.org/10.5194/gmd-8-3071-2015

Gaspar, P., Grégoris, Y., & Lefevre, J. (1990). A simple eddy kinetic energy model for simulations of the oceanic vertical mixing: Tests at station papa and long-term upper ocean study site. *Journal of Geophysical Research*, *95*(C9), 16179–16193. https://doi.org/10.1029/jc095ic09p16179

Gent, P. R., & McWilliams, J. C. (1990). Isopycnal mixing in ocean circulation models. *Journal of Physical Oceanography*, *20*(1), 150–155. https://doi.org/10.1175/1520-0485(1990)020<0150:imiocm>2.0.co;2

Hartmann, N. B., Hüffer, T., Thompson, R. C., Hassellöv, M., Verschoor, A., Daugaard, A. E., et al. (2019). Are we speaking the same language? Recommendations for a definition and categorization framework for plastic debris. *Environmental Science & Technology*, *53*(3), 1039–1047. https://doi.org/10.1021/acs.est.8b05297

Jambeck, J. R., Geyer, R., Wilcox, C., Siegler, T. R., Perryman, M., Andrady, A., et al. (2015). Plastic waste inputs from land into the ocean. *Science*, *347*(6223), 768–771. https://doi.org/10.1126/science.1260352

Khatmullina, L., & Isachenko, I. (2017). Settling velocity of microplastic particles of regular shapes. *Marine Pollution Bulletin*, *114*(2), 871–880. https://doi.org/10.1016/j.marpolbul.2016.11.024

Kooi, M., Nes, E. H. V., Scheffer, M., & Koelmans, A. A. (2017). Ups and downs in the ocean: Effects of biofouling on vertical transport of microplastics. *Environmental Science & Technology*, *51*(14), 7963–7971. https://doi.org/10.1021/acs.est.6b04702

Lau, W. W. Y., Shiran, Y., Bailey, R. M., Cook, E., Stuchtey, M. R., Koskella, J., et al. (2020). Evaluating scenarios toward zero plastic pollution. *Science*, *369*(6510), 1455–1461. https://doi.org/10.1126/science.aba9475

Lebreton, L.-M., Greer, S., & Borrero, J. (2012). Numerical modelling of floating debris in the world's oceans. *Marine Pollution Bulletin*, *64*(3), 653–661. https://doi.org/10.1016/j.marpolbul.2011.10.027

Lobelle, D., Kooi, M., Koelmans, A. A., Laufkötter, C., Jongedijk, C. E., Kehl, C., & van Sebille, E. (2021). Global modeled sinking characteristics of biofouled microplastic. *Journal of Geophysical Research: Oceans*, *126*(4), e2020JC017098. https://doi.org/10.1029/2020jc017098

Marshall, J., Adcroft, A., Hill, C., Perelman, L., & Heisey, C. (1997). A finite-volume, incompressible Navier Stokes model for studies of the ocean on parallel computers. *Journal of Geophysical Research*, *102*(C3), 5753–5766. https://doi.org/10.1029/96JC02775

Marshall, J., Hill, C. N., Perelman, L., & Adcroft, A. (1997). Hydrostatic, quasi-hydrostatic, and nonhydrostatic ocean modeling. *Journal of Geophysical Research*, *102*(C3), 5733–5752. https://doi.org/10.1029/96JC02776

Maximenko, N., Hafner, J., & Niiler, P. (2012). Pathways of marine debris derived from trajectories of Lagrangian drifters. *Marine Pollution Bulletin*, *65*(1–3), 51–62. https://doi.org/10.1016/j.marpolbul.2011.04.016

Mensa, J. A., Özgökmen, T. M., Poje, A. C., & Imberger, J. (2015). Material transport in a convective surface mixed layer under weak wind forcing. *Ocean Modelling*, *96*, 226–242. https://doi.org/10.1016/j.ocemod.2015.10.006

Mountford, A. S., & Morales Maqueda, M. A. (2019). Eulerian modeling of the three-dimensional distribution of seven popular microplastic types in the global ocean. *Journal of Geophysical Research: Oceans*, *124*(12), 8558–8573. https://doi.org/10.1029/2019jc015050

Mountford, A. S., & Morales Maqueda, M. A. (2021). Modeling the accumulation and transport of microplastics by sea ice. *Journal of Geophysical Research: Oceans*, *126*(2), e2020JC016826. https://doi.org/10.1029/2020jc016826

Niiler, P. (2001). The world ocean surface circulation. In *Ocean Circulation and Climate—Observing and Modelling the Global Ocean* (pp. 193–204). Elsevier. https://doi.org/10.1016/s0074-6142(01)80119-4

Oguri, K., Kawamura, K., Sakaguchi, A., Toyofuku, T., Kasaya, T., Murayama, M., et al. (2013). Hadal disturbance in the Japan trench induced by the 2011 Tohoku–Oki earthquake. *Scientific Reports*, *3*(1), 1915. https://doi.org/10.1038/srep01915

Redi, M. H. (1982). Oceanic isopycnal mixing by coordinate Rotation. *Journal of Physical Oceanography*, *12*(10), 1154–1158. https://doi.org/10.1175/1520-0485(1982)012<1154:OIMBCR>2.0.CO;2

Richon, C., Gorgues, T., Paul-Pont, I., & Maes, C. (2022). Zooplankton exposure to microplastics at global scale: Influence of vertical distribution and seasonality. *Frontiers in Marine Science*, *9*, 947309. https://doi.org/10.3389/fmars.2022.947309

Sun, Y., Bakker, T., Ruf, C., & Pan, Y. (2023). Effects of microplastics and surfactants on surface roughness of water waves. *Scientific Reports*, *13*(1), 1978. https://doi.org/10.1038/s41598-023-29088-9

Sunil, S., Bhagwat, G., Vincent, S. G. T., & Palanisami, T. (2024). Microplastics and climate change: The global impacts of a tiny driver. *Science of the Total Environment*, *946*, 174160. https://doi.org/10.1016/j.scitotenv.2024.174160

the NOAA Marine Debris Program. (2024). Microplastics. Retrieved from https://marinedebris.noaa.gov/what-marine-debris/microplastics

Tseng, Z. (2025). *reproduce-eccov4r4-online-68o*. Zenodo. https://doi.org/10.5281/zenodo.16903982

van Sebille, E., England, M. H., & Froyland, G. (2012). Origin, dynamics and evolution of ocean garbage patches from observed surface drifters. *Environmental Research Letters*, *7*(4), 044040. https://doi.org/10.1088/1748-9326/7/4/044040

Wunsch, C., & Heimbach, P. (2007). Practical global oceanic state estimation. *Physica D: Nonlinear Phenomena*, *230*(1–2), 197–208. https://doi.org/10.1016/j.physd.2006.09.040

Yang, D., Chamecki, M., & Meneveau, C. (2014). Inhibition of oil plume dilution in Langmuir ocean circulation. *Geophysical Research Letters*, *41*(5), 1632–1638. https://doi.org/10.1002/2014gl059284



21699291, 2025, 9, Downloaded from https://agupubs.onlinelibrary.wiley.com/doi/10.1029/2025JC023272 by University Of Michigan Library, Wiley Online Library on [30/08/2025]. See the Terms and Conditions (https://onlinelibrary.wiley.com/terms-and-conditions) on Wiley Online Library for rules of use; OA articles are governed by the applicable Creative Commons License